AMS Home   Journals Home   Journal Archive   Subscribe   For Authors   Help   Advanced Search   Search [Go]

Full Text View

Upper-Ocean Turbulence during a Westerly Wind Burst: A Comparison of Large-Eddy Simulation Results and Microstructure Measurements

Eric D. Skyllingstad

Pacific Northwest National Laboratory, Marine Sciences Laboratory, Sequim, Washington

W. D. Smyth, J. N. Moum, and H. Wijesekera

College of Oceanic and Atmospheric Sciences, Oregon State University, Corvallis, Oregon

ABSTRACT

The response of the upper ocean to westerly wind forcing in the western equatorial Pacific was modeled by means of large-eddy simulation for the purpose of comparison with concurrent microstructure observations. The model was initialized using currents and hydrography measured during the Coupled Ocean–Atmosphere Response Experiment (COARE) and forced using measurements of surface fluxes over a 24-h period. Comparison of turbulence statistics from the model with those estimated from concurrent measurements reveals good agreement within the mixed layer. The shortcomings of the model appear in the stratified fluid below the mixed layer, where the vertical length scales of turbulent eddies are limited by stratification and are not adequately resolved by the model. Model predictions of vertical heat and salt fluxes in the entrainment zone at the base of the mixed layer are very similar to estimates based on microstructure data.

Table of Contents:

Options:
- Create Reference
- Email this Article
- Add to MyArchive
- Search AMS Glossary

Search CrossRef for:
- Articles Citing This Article

Search Google Scholar for:
- Eric D. Skyllingstad
- W. D. Smyth
- J. N. Moum

1. Introduction

Large-eddy simulation (LES) models have been used extensively in studies of atmospheric boundary layers [see Wyngaard and Peltier (1996) and Mason (1994) for reviews] and have recently been applied to help understand ocean boundary layer processes (Siegel and Domaradzki 1994; Skyllingstad and Denbo 1995; Denbo and Skyllingstad 1996; Wang et al. 1996; McWilliams et al. 1997; Skyllingstad et al. 1996; Wang et al. 1998). The idea behind LES is to directly simulate the largest and

- H. Wijesekera

most energetic turbulent eddies and parameterize motions smaller than the model grid spacing. Because LES models resolve the largest turbulent motions, they can provide useful information on mixing processes such as convection or Langmuir circulations, provided that the scale of the process is adequately bracketed by the model grid spacing and the domain size. A key requirement in the use of LES models is that the spatial resolution includes the scales of the energy-containing eddies so that the smallest resolved motions lie within an inertial subrange. Where finite computational resources prevent satisfaction of this requirement, the validity of the results is questionable.

Direct calculation of the largest turbulent eddies in LES is what sets these models apart from more simplified turbulence modeling approaches, such as bulk mixed layer models (e.g., Kraus and Turner 1967; Garwood, 1977; Price et al. 1986), high-order turbulence closure models (e.g., Mellor and Yamada 1982), or eddy diffusion models (e.g., Large et al. 1994). In comparison to these approaches, assumptions regarding the formation of turbulence and the transport of momentum and scalars by turbulent eddies are minimized in LES, although parameterization of unresolved turbulent motions is still required. Because LES has fewer assumptions, the technique should provide a more accurate simulation of turbulence in comparison to typical parameterizations of the ocean boundary layer. However, few ocean LES results have been tested against measured ocean turbulence. In this paper, we assess the validity of an LES model of the upper ocean via comparisons with concurrent microstructure measurements.

Our spatial resolution is more than adequate within the mixed layer where the most energetic eddies are much larger than the grid spacing. In the stably stratified fluid underlying the mixed layer, however, the dominant eddies are too small to be resolved by the grid, and the assumptions underlying the subgrid-scale (SGS) model become invalid. Comparisons with observational data allow us to assess the impact of this underresolution on the realism of the model output. We will see that turbulent dissipation rates (which are dominated by small eddies) are unrealistically small in the stratified zone below the mixed layer, but that turbulent heat fluxes (which are driven by the largest eddies) remain quite realistic.

We examine turbulent processes in the western tropical Pacific oceanic boundary layer during a westerly wind burst (WWB). This wind event took place during the intensive observation period of Tropical Oceans Global Atmosphere Coupled Ocean–Atmosphere Response Experiment (TOGA COARE), and its effect on the vertical structure of the ocean boundary layer has been documented by Smyth et al. (1996a,b: hereafter SHM1, SHM2). The deep mixed layer structure (60 to 100 m) and strong surface forcing provides a unique ocean environment for the application of LES, combining both strong buoyancy forcing from surface fluxes and a sheared current structure. Extensive microstructure measurements taken during this particular event provide us with an opportunity to examine the correspondence between measured and modeled ocean turbulence.

While LES data comparisons have been performed in the atmospheric context, such comparisons have not been attempted in the ocean before now. The present comparison effort differs from prior atmospheric comparisons in two major respects: the essential physics of the turbulent flow being simulated, and the nature of the observational data available for comparison. The equatorial upper ocean exhibits stable stratification and intense zonal shear. In contrast, most applications of LES models in the atmosphere have concentrated on low shear conditions, where buoyancy provides the dominant forcing of turbulent eddies. Comparisons with both laboratory (e.g., Deardorff and Willis 1985) and field data (Lenschow et al. 1980; Kaimal et al. 1976) have shown the range of validity of these simulations.

Measured atmospheric variables have typically included turbulent velocity and temperature. These data have been used in LES validation, for example, by comparing vertical profiles of the mean turbulent kinetic energy. In the oceanic case, fundamental differences between the variables computed by the LES and those observed complicate the task of comparing results. For example, microstructure profilers do well at resolving vertical variability on scales less than a few meters and are therefore most effective for measuring quantities that have variance concentrated in these scales, such as the kinetic energy dissipation rate. In contrast, large-eddy simulations on the scales of interest here are currently limited to a spatial resolution of a few meters and are thus more suited to the calculation of quantities like the turbulence kinetic energy (TKE), which has a spectrum that peaks at larger scales. Although TKE can now be computed from ocean turbulence measurements (Moum 1996a), these measurements were not routinely implemented in COARE. The TKE dissipation rate that was measured provides our basis for comparison. In fact, we consider dissipation rate to be more telling because the LES computation requires both adequate resolution of the turbulence scale and proper parameterization of the small scales that dominate the dissipation rate. Methods for inferring dissipation rate from LES are described in the appendix.

Our modeling methods will be described in section 2. In section 3, we present an overview of the evolution of the simulated flow and describe in detail the physical mechanisms that govern production and damping of turbulence in the model. In section 4, we discuss comparisons between model results and observations, focusing on turbulent dissipation rates for kinetic energy and temperature variance. A statistical comparison between the model turbulent dissipation rates and observations is presented as a test of the model accuracy in reproducing the boundary layer turbulent structure. An analysis of the turbulent length scales is presented in section 5 and is used to help explain discrepancies noted in the statistical analysis of turbulence dissipation rates. Comparison of heat and salinity fluxes through the mixed layer base (MLB) is

2. Method

In this section, we discuss our simulation methods. We begin with a description of the LES model, then discuss the incorporation of oceanographic and meteorological data into the model via initial and boundary conditions.

a. Large-eddy simulation model

The LES model used in this study is described in detail in Denbo and Skyllingstad (1996) and Skyllingstad and Denbo (1995). Briefly, the model is based on the Deardorff (1980) equations of motion, with modifications made to account for the equation of state for seawater and wave–current interaction using the Craik and Leibovich (1976) Stokes drift vortex force. The model equations are

$$\frac{\partial u_i}{\partial t} = -u_j \frac{\partial u_i}{\partial x_j} - \frac{\partial}{\partial x_j}\langle u_i'' u_j'' \rangle - \frac{\partial \tilde{P}}{\partial x_i} + \varepsilon_{ijk}(u_j + u_j^s)f_k$$

$$- \delta_{i3} g \frac{\rho'}{\rho_0} + \varepsilon_{ijk} u_j^s \zeta_k + \alpha \partial^{12} u_i \qquad (1)$$

$$\frac{\partial \varphi}{\partial t} = -u_i \frac{\partial \varphi}{\partial x_i} - \frac{\partial}{\partial x_i}\langle u_i'' \varphi \rangle, \qquad (2)$$

where

$$\langle u_i'' u_j'' \rangle = -K_m \left(\frac{\partial u_i}{\partial x_j} + \frac{\partial u_j}{\partial x_i} \right), \qquad \langle u_i'' \varphi \rangle = -K_h \frac{\partial \varphi}{\partial x_i},$$

$$\tilde{P} = \frac{P}{\rho_0} + \frac{2}{3}\overline{q^2}, \qquad \qquad \zeta_k = \varepsilon_{kij}\left(\frac{\partial u_j}{\partial x_i} \right).$$

Here u_i are the Cartesian velocity components, x_i are the Cartesian distance, t is time, g is the acceleration of gravity, f_k is the kth component of the earth's vorticity, δ_{i3} is the Kronecker delta, φ is a scalar field such as temperature or salinity, P is the pressure, K_m is the subgrid-scale eddy viscosity, K_h is the subgrid-scale eddy diffusivity, $\overline{q^2}$ is the subgrid-scale turbulent kinetic energy, u^s is the Stokes drift velocity, ζ_k is the kth component of vorticity, and $\alpha \partial^{12} u_i$ is a twelfth-order filter with filter coefficient $\alpha = 0.2$ to remove a $2\Delta x$ artifact of the flux differencing scheme (see Denbo and Skyllingstad 1996). The filter is only applied once every 100 time steps and has a minimal impact on the resolved scale motions. In (1) ε_{ijk} represents the standard antisymmetric tensor and should not be confused with the scalar TKE dissipation rate ε. Double primes signify subgrid-scale quantities; angle brackets represent a spatial average over a grid cell. Density is calculated as $\rho = \rho(T, s, P)$, using the IES 80 equation of state (UNESCO 1981, p. 24).

The model horizontal boundaries are periodic, and a radiation condition is imposed at the lower boundary. For the present work, the Asselin filtered, centered-in-time differencing scheme was replaced with the third-order Adams–Bashforth scheme described in Durran (1991). The flux momentum scheme described by Clark (1977) was also incorporated. These changes were necessary to avoid severe smoothing caused by the Asselin time filter in the strong background flow of the equatorial region and to ensure conservation of kinetic energy. Scalar advection in the model was also improved by replacing the previously used Collela (1990) scheme with a version of the corner transport upwind scheme described in Leveque (1996). The model was also modified to account for the significant transfer of shortwave radiation through the top 100 m of the warm pool water column. Time-averaged transparency observations from COARE (Siegel et al. 1995) were used to parameterize this effect and to determine the direct heating from shortwave radiation at each model level.

To increase the computational efficiency of the model, we implemented a new subgrid parameterization based on the structure function scheme of Métais and Lesieur (1992). The scheme provides a fit between the resolved turbulence structure and an assumed Kolmogorov TKE spectrum at subgrid scales. Eddy viscosity is only nonzero if resolved-scale

motions exist in the flow field and have small-scale variability. The structure function method yields the eddy viscosity

$$K_m = 0.063\Delta x(\overline{F}(\mathbf{x}))^{1/2}, \quad (3)$$

where the velocity structure function $\overline{F}(\mathbf{x})$ is approximated by the modulus of the velocity differences between adjacent grid points, or

$$\overline{F}(\mathbf{x}) = \overline{\|\mathbf{u}(\mathbf{x}) - \mathbf{u}(\mathbf{x} + \mathbf{r})\|^2}_{\|\mathbf{r}\|=\Delta x},$$

and $\mathbf{u}$ is the three-component velocity vector. Because we are using a staggered grid (Arakawa C), the horizontal velocities are first averaged to the scalar location at the grid center. The average operator (overbar) is then taken over the six adjoining grid points. In the present implementation, the horizontally averaged flow is removed before the structure function is computed. The turbulent diffusivity is represented as $K_h = K_m/Pr_t$, where Pr_t is the turbulent Prandtl number. Following Métais and Lesieur (1992), we give Pr_t the value 0.6. Comparison of velocity spectra produced using the structure function model to the original Deardorff (1980) subgrid parameterization shows only minor differences between the two methods; however, the new scheme makes more efficient use of computational resources.

The Stokes drift velocity, $\mathbf{u}^s$, is parameterized using

$$\mathbf{u}^s = 11.5u*\frac{\boldsymbol{\tau}}{|\tau|}\left(\exp\left[4\pi\left(\frac{z}{\lambda}\right)\right]\right), \quad (4)$$

where $\boldsymbol{\tau}$ is the surface wind stress vector, τ is the wind stress magnitude, $u* = (|\tau|/\rho)^{1/2}$ is the friction velocity, ρ is the density, z is the depth, and λ is the surface wave wavelength (Li and Garrett 1993). Wave estimates from sonar data (S. Hill and D. Farmer, 1995, personal communication) indicate a peak in the wave height spectrum for waves with period of 4–5 s. Therefore, we assumed a constant λ of 30 m for both experiments, representing average surface wave conditions during the WWB.

A horizontal domain size of 384 m × 384 m, and depth of 96 m was used, with a uniform grid spacing of 1.5 m with a time step of 1.2 s. Simulations were performed on a Thinking Machines CM-5 and required 2.2 system hours to complete one simulated hour using a dedicated 256-nodes partition with vector processing units.

b. Boundary and initial conditions

To minimize the influence of variable external forcing, such as rainfall or wind gustiness, we selected a case from a period of uniform surface forcing that began on 31 December 1992. As shown in Fig. 1 ◐, weather conditions during this time period were characterized by steady winds with little precipitation and a consistent diurnal surface heat flux cycle. Consequently, the overall ocean turbulence structure exhibited a strong diurnal signal with a deepening mixed layer during the evening and a rapid decrease in turbulence during daytime solar heating.

Our experiment examines a 24-h time period starting at 0000 UTC 31 December 1992, covering the surface heat flux transition at both sunset and sunrise. The temperature and current structure for 31 December 1992 at 0000 UTC is presented in Fig. 2 ◐, and the surface heat and wind stress for the following 24 h in Fig. 3 ◐. Fluxes of heat, salinity, and momentum are prescribed at the top model grid points by replacing the finite difference subgrid diffusion at the upper surface with a flux boundary condition (see Skyllingstad and Denbo 1995 for details).

3. Modeled and measured turbulence response to surface forcing

Before proceeding to a detailed statistical comparison of modeled and measured turbulence, we present an overview of the evolution of the upper-ocean currents and hydrography in response to the observed surface forcing. We describe the time history of the modeled and measured fields, the spatial structure of the turbulence produced by the model, and the physical mechanisms that govern the development of the modeled turbulence.

a. Time evolution of modeled and measured fields

To illustrate the response of the model to changing surface forcing, we first examine the observed and modeled

temperature T, salinity S, and horizontal velocity components u and υ (Fig. 3 ⊙). The measured fields contain long period tidal fluctuations, internal waves, and large-scale traveling disturbances (e.g., at hours 11–14 and after hour 16; Fig. 3 ⊙) that affect the mixed layer depth but do not significantly interact with high-frequency motions that are of interest here (i.e., they cause vertical displacements but do not significantly affect the magnitude of either turbulent dissipation rates or irreversible transports of heat or salt). We define the mixed layer (ML) as the layer in which the potential density exceeds its surface value by less than 0.01 kg m^{-3}. Also shown in Fig. 3 ⊙ are the surface heat flux and wind stress for comparison with the mixed layer variables.

Spinup of the model mixed layer turbulence takes approximately 3 hours. Following this, the mixed layer depth is relatively constant until the surface heat flux switches sign from heating to cooling at around hour 5. Between hours 5 and 8, the mixed layer deepens rapidly and then again remains relatively constant until surface warming is reestablished at hour 22.

The modeled temperature evolution (Fig. 3c ⊙) is in good agreement with observations (Fig. 3b ⊙), showing gradual cooling in response to the surface heat flux (Fig. 3a ⊙) and to entrainment at the base of the ML. In both the model and the observations, ML salinity increased slightly (rainfall was minimal). Comparison of currents is more complex. The near-surface zonal current (Figs. 3g, 3h ⊙) accelerated initially in response to wind forcing (Fig. 3f ⊙). In the model, this acceleration persisted for the duration of the simulation, while the observed zonal current decelerated abruptly near hour 12. Modeled meridional currents (Fig. 3k ⊙) show a weak northward trend, possibly caused by Coriolis effects, while the observed meridional current (Fig. 3j ⊙) accelerated toward the south, consistent with the sign of the wind stress (Fig. 3i ⊙). It is evident that observed currents are strongly affected by large-scale variability, which the model cannot reproduce because of its limited horizontal extent. We will see later that the absence of large-scale wave motions in the model degrades the accuracy of the modeled turbulence in the later stages of the simulation.

Profiles of the simulated squared current shear Sh^2, Brunt-Väisälä frequency N, and Richardson number Ri, are shown in Fig. 4 ⊙ at hours 3 and 16, representing the initial state after model spinup, and the mixed layer during nightime cooling, respectively. The current shear, Brunt–Väisälä frequency, and Richardson number are defined as

$$Sh^2 \equiv \left(\frac{\partial u}{\partial z}\right)^2 + \left(\frac{\partial \upsilon}{\partial z}\right)^2, \qquad N^2 \equiv -\frac{g}{\rho_0}\frac{\partial \sigma_\theta}{\partial z}, \qquad Ri \equiv \frac{N^2}{Sh},$$

where σ_θ is the potential density and ρ_o is a constant reference density. Initially, the simulated profiles have a number of layers of reduced stability that are a reflection of the observed density and velocity fields. Here Ri approaches ¼ within the top $\sim$ 5 m and at various depths in the ML interior and at the MLB. At hour 16, surface cooling produces a deeper region of low Ri in the upper mixed layer, with the lower half of the ML characterized by $Ri > $ ¼. The increase in Ri beginning at 55–60 m is a result of restratification from entrained thermocline water and reduced shear because of increased turbulence from surface forcing.

b. Spatial structure of the modeled fields

Many of the time-dependent features noted above can be related to physical processes that are visible in the vertical velocity field as shown in Fig. 5 ⊙. This plot shows three differing regimes of turbulence corresponding to the complex vertical ε structure evident in Fig. 1 ⊙. Near the surface, vertical motions are dominated by Langmuir circulations that result from the interaction of the surface wave Stokes drift with the wind-forced current shear. These circulations are of order 10–20 m in horizontal scale and tend to cluster along larger-scale convergence zones (100-m scale) that are forced by the middepth longitudinal circulations visible at 20 m. Also important near the surface are enhanced turbulent eddies produced by the wind stress and resulting shear flow. This turbulence is in part responsible for the enhanced near-surface ε, as demonstrated by similarity scaling (e.g., Shay and Gregg 1986). The middepth circulations are similar to roll vortices simulated in atmospheric boundary layer shear flows (Moeng and Sullivan 1994; Coleman et al. 1994). The scale of the eddies contracts at the MLB, where the effects of shear instability dominate the turbulent velocity fields. These perturbations are 50–100 m in scale and have a wavelike appearance, for example, as shown at 65-m depth in Fig. 5 ⊙. It is likely that the structure of these disturbances is strongly modified by density stratification, resulting in both wavelike and turbulent behavior.

c. The mechanics of modeled boundary layer turbulence

A fundamental strength of LES modeling is the ability to calculate the individual sources and sinks of TKE. Here we define the horizontally averaged, resolved TKE as

where the overbar denotes a horizontal average and the prime denotes the departure from that average. The evolution equation for TKE is derived by multiplying (1) by u'_i and averaging over the horizontal domain, yielding

$$\frac{\partial E}{\partial t} = \frac{\overline{\partial u'_3 E}}{\partial x_3} - \overline{u'_i u'_3 \frac{\partial \bar{u}_i}{\partial x_3}} - \overline{u'_i \left(\frac{\partial \tilde{P}}{\partial x_i}\right)} - \overline{u'_i \left(\frac{\partial \langle u''_i u''_j \rangle}{\partial x_j}\right)}$$

$$- \overline{u'_3 g \frac{\rho'}{\rho_0}} + \overline{u'_i (\varepsilon_{i,j,k} u^s_j \zeta_k)'} + \overline{u'_i (\alpha \partial^{12} u_i)'}. \qquad (6)$$

The seven terms on the right-hand side of (6) represent, in order, vertical advection, shear production, pressure transport, subgrid-scale dissipation, buoyancy production, Stokes vortex force, and filter dissipation. The most significant of these terms are displayed as functions of time and depth in Fig. 6 ⊙═, along with the mixed layer depth. Near the surface, sources of turbulence are linked primarily to the surface wind stress through the shear production and Stokes vortex force terms and through the surface heat flux, which drives the buoyancy production. Although the most vigorous energy exchanges occur near the surface, the scaling employed in Fig. 6 ⊙═ reveals processes that govern mixing throughout the boundary layer.

During the first 5 h of the simulation period, typical afternoon conditions prevailed. The surface buoyancy flux was stabilizing, but strong winds maintained a ML depth of 30–40 m. Near hour 5, the surface buoyancy flux changed sign, initiating the evening deepening of the ML. The ML depth increased to nearly 60 m over the subsequent 3 h. TKE increased rapidly during this time (Fig. 6a ⊙═). Turbulence was created in the ML interior via shear production (Fig. 6b ⊙═) then advected downward to the base of the ML (Fig. 6d ⊙═). During this time, TKE increase near the MLB was limited by the effects of buoyancy (Fig. 6c ⊙═) and dissipation (Fig. 6f ⊙═). Subsequently, the shear production rate decreased and TKE decreased (Fig. 6a ⊙═, hour 9) to a quasi-equilibrium level that persisted for the rest of the night. The physics of that quasi-equilibrium state will be described in detail below. Near hour 21, the morning reversal of the buoyancy flux caused a rapid decrease in TKE. This process was greatly amplified by a small rain shower (cf. Smyth et al. 1997). Buoyancy production changed sign as surface warming and freshening stabilized the near-surface stratification. Shear production and vertical advection were arrested but resumed after the rain stopped.

We turn now to a detailed examination of the balance of TKE sources and sinks that maintained the quasi-equilibrium state that persisted from approximately hour 11 to hour 20 (Fig. 7 ⊙═). We find it useful to imagine the boundary layer as consisting of three sublayers: a near-surface region where mixing is generated by air–sea interactions (-10 m $< z < 0$ m), a strongly sheared entrainment layer adjacent to the thermocline where turbulence is generated locally by the shear and lost to buoyancy production (-70 m $< z < -40$ m), and a central region that is influenced by both the remote effects of air–sea interactions and the local effects of shear and buoyancy production (-40 m $< z < -10$ m).

We focus first on near-surface processes, that is, those occurring in the upper $\sim$ 10 m. Because of the cooling effect of the surface heat flux, the near-surface region is characterized by weakly unstable stratification. As a result, buoyancy acts as an energy source in this region of the water column (Fig. 7c ⊙═). Buoyancy forcing is relatively weak, however, in comparison with other TKE source terms. The latter include the Stokes vortex force (Fig. 7a ⊙═) and the shear production (Fig. 7b ⊙═), which both act vigorously to generate turbulence in the top few meters. The concentration of the Stokes drift effect near the surface is consistent with the results of Skyllingstad and Denbo (1995) and McWilliams et al. (1997), who show that the vortex force contributes to the interior turbulence budget mainly as a boundary condition. Two vertical flux terms act to redistribute energy generated at the surface. The pressure flux (Fig. 7e ⊙═) is directed downward, removing energy from the surface and distributing it over the upper $\sim$ 15 m. The advective flux (Fig. 7d ⊙═) distributes surface-generated kinetic energy throughout the mixed layer. Finally, the transfer of energy into subgrid-scale motions (Fig. 7f ⊙═) represents a strong sink of kinetic energy in the upper 10 m.

In the entrainment zone at the base of the nocturnal ML ($z \sim$ 40 to 70 m), turbulence is generated mostly by shear production (Fig. 7b ⊙═), with a contribution by downward advection of TKE from the ML interior (Fig. 7d ⊙═). Some of the kinetic energy thus created is converted to potential energy due to the stable stratification (Fig. 7c ⊙═); most of the remainder is dissipated by subgrid-scale motions (Fig. 7f ⊙═).

In the central region of the nocturnal mixed layer, between 10 and 40 m, we observe an intermediate regime in which turbulence is generated by a combination of processes. Buoyancy production (Fig. 7c ⊙═) is significant in the upper part of this layer but gives way to shear production deeper down. Vertical advection (Fig. 7d ⊙═) of TKE plays a very significant role, transporting surface-generated turbulence downward into the ML. A plausible interpretation is that the combination of

shear and convection generates large eddies that have a length scale restricted only by the depth of the mixed layer (cf. Fig. 5 ⊙) and that those large eddies act in turn to advect turbulent fluid from the surface into the interior of the mixed layer. The dominant TKE sink in this region is the subgrid-scale dissipation (Fig. 7f ⊙).

The dominant terms in the pycnocline below 70 m are those representing shear production and pressure transport. This suggests that disturbance energy is created by shear instability and subsequently radiated vertically in the form of internal waves (cf. Sun et al. 1998, manuscript submitted to *J. Geophys. Res.*). Over limited areas near the MLB, these waves are strong enough to break and promote significant mixing, as discussed in section 5. However, most of the wave energy propagates out of the model domain through the open bottom boundary and does not appear to have a significant role in creating turbulence.

In interpreting the present results, we must keep in mind that our model neglects a potentially important source of TKE, namely breaking surface waves. The appropriate parameterization for turbulence due to wave breaking is a current research topic. However, we can estimate its importance using a simple model described by Craig and Banner (1994). Craig and Banner solved a simplified TKE equation for a case in which downward (turbulent) diffusion of TKE due to wave breaking is balanced by viscous dissipation. The surface TKE flux was taken to be proportional to the cube of the friction velocity u ∗. Terray et al. (1996) provided the expression $\alpha = 0.5 C_p/u$ ∗ for the proportionality constant, where C_p is the phase velocity of the dominant surface waves. The result is an estimate of ε_w, the dissipation rate that is needed to balance turbulent diffusion of TKE from wave breaking:

$$\varepsilon_w = \frac{1.2 C_p u_*^2}{z_o}\left(1 + \frac{z}{z_o}\right)^{-3.4}. \tag{7}$$

The roughness depth z_o is similar to the significant wave height, which we estimate from visual observations to be 1 m. We set C_p to 6.8 m s^{-1}, consistent with our assumed wavelength of 30 m. The depth dependence of ε_w using (7), along with the SGS dissipation rate, is presented in Fig. 8 ⊙ for the nocturnal quasi-equilibrium period from 11 to 20 h. Also shown is the surface similarity scaling based on the surface wind stress, namely,

$$\varepsilon_s = \frac{u_*^3}{\kappa z}, \tag{8}$$

where κ is the von Kármán coefficient and is set equal to 0.4. Modeled dissipation rates agree with (8) to within a factor of 2 over the upper 50 m.

In the upper few meters, ε_w exceeds the dissipation rate produced by our model by more than an order of magnitude. However, ε_w decreases rapidly with depth and is comparable to the model dissipation rate by 10 m, the shallowest depth at which microstructure data is available for comparison. This suggests that wave-breaking effects, while potentially dominant in the upper few meters, will have little impact at the depths where our comparisons are conducted. Recall, however, that in Craig and Banner's model, surface-generated TKE is fluxed downward only by its own turbulent diffusivity. In the nocturnal mixed layer, other processes, such as orbital motions due to surface waves (including the much longer wavelength swell, e.g., Anis and Moum 1995) and large eddies due to shear and convection, have the potential to enhance downward transport of surface-generated TKE. Therefore, we cannot rule out the possibility that our model will underestimate ML turbulence due to the neglect of surface wave-breaking effects.

As shown by the foregoing analyses, the LES model can provide a means for understanding the processes that control the formation and decay of turbulence and entrainment at the MLB. Correctly parameterizing these processes in one-dimensional mixed layer models is critical for accurate prediction of mixed layer properties. Some of the assumptions made in one-dimensional parameterizations can be examined using the LES results. For example, in bulk layer models, such as Kraus and Turner (1967) or Garwood (1978), the mixed layer is assumed to have uniform characteristics and a growth rate that is controlled by engulfment of thermocline water by turbulent eddies. In general, mixed layer scalar properties predicted by the LES model are uniform through the mixed layer, supporting the use of a bulk layer approach. However, this is not the case for momentum (Fig. 3 ⊙), or for the terms in the TKE budget, which have significant structure throughout the mixed layer. Of critical importance in bulk layer models is an accurate estimation of the entrainment properties at the MLB. Bulk layer models typically assume that increased ML TKE is transferred to ML potential energy as heavier thermocline water is engulfed by mixed layer eddies. Thus, turbulent energy generated by surface fluxes is balanced completely by the upward transport of cold or more saline thermocline water, without dissipation. This assumption is in contrast to the LES results that show a significant source of TKE at the MLB through shear production, with comparable dissipation rates. However, as shown by the TKE budget, much of the shear generation of turbulence at the MLB is offset by increased dissipation. This

may explain why bulk layer models frequently produce reasonable mixed layer entrainment rates, albeit for the wrong reasons.
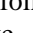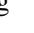
One-dimensional models that do not assume uniform mixed layer properties represent mixed layer properties in a manner that is more consistent with the present results. For example, most of the budget terms presented here are individually parameterized in the Mellor and Yamada (1982) and Kantha and Clayson (1994) higher-order closures, yielding vertical mixing that is not assumed constant through the mixed layer. The K profile (KPP) model described in Large et al. (1994) simulates turbulence in the mixed layer by applying a profile of eddy viscosity that is nonuniform in the vertical and allows for nonlocal transport as is produced by eddies that span the depth of the ML. Each of these one-dimensional models attempts to account for the nonuniform behavior of ML turbulence, and in general, have lead to improved estimates of ML properties in comparison to bulk layer models (see, e.g., Large et al. 1994).

Further field experiments and improved measurement capabilities are needed to verify the roles of the individual TKE budget terms. Of the terms governing the evolution of TKE, we have only succeeded in making fairly routine measurements of ε. We expect to soon see routine measurements of TKE (Moum 1996a) and perhaps of buoyancy flux (Moum 1996b). However, little progress has been made in measuring other terms to date.

4. Comparison of measured and modeled turbulent dissipation rates

We turn now to statistical comparisons between measured and modeled dissipation rates. Because of the extreme spatial and temporal intermittency of these quantities, we do not expect good correspondence between point values. Rather, we expect that statistical properties of subsamples, taken over suitable intervals of space and time, should correspond. The bulk of our analyses in this section are focused on statistical properties of subsamples spanning 6 m in depth and 1 h or more in time. We preface these analyses with a direct, qualitative comparison of measured and modeled dissipation rates as functions of time and depth (Fig. 9 ⬤).

The model run was initiated in early afternoon local time, in order to give model turbulence time to spin up before the evening deepening of the mixed layer. Thus, we do not expect good comparison in the first few hours of the run. Aside from this, the main qualitative features of the variability of the dissipation rates were reproduced accurately by the model: ε was largest near the surface and within a layer that deepened to cover the upper 60 m by hour 8 (Fig. 9a ⬤). After hour 10, ε values in the mixed layer decreased significantly, both in the model and in the observations. Heaving of the nocturnal mixed layer base due to internal waves is visible in the observations, but not in the model results, because such waves are not locally generated and have horizontal scales much too large to be accommodated in the model domain. In both the model data and the measurements, high ε values extend about 10 m below the ML base. Below this region, model ε values are smaller than measured values, typically by an order of magnitude. Temperature variance dissipation rates (Fig. 9b ⬤) are determined not only by the intensity of the turbulence, but also by the strength of the ambient thermal stratification. Therefore, compared with ε, χ is relatively weak within the mixed layer and strong in the thermocline. The overall structure of χ within the mixed layer was well reproduced by the model. However, the model required several hours of spinup time before χ values in the thermocline became comparable to observations. Even after this spinup period, we observe significant discrepancies. Measured χ takes large values ($\sim 10^{-6}$ K^2 kg^{-1} s^{-1}) in a layer extending for about 20 m below the ML base, then decreases dramatically, then increases again. This structure is not reproduced in the model output, which is dominated by values intermediate between the extremes appearing in the measurements. Sunrise occurred near hour 20 (Fig. 3a ⬤). After this time, both measured and modeled dissipation rates decayed noticeably within the ML. Below the MLB, however, measured dissipation rates remained significantly stronger than those generated by the model.

Direct comparison of the model statistics with measurements is complicated by the limited number of observation points and low temporal resolution inherent with the observed data. Sampling intervals for microstructure observations were typically 6–9 minutes. Dissipation rates were estimated as 1-m vertical averages, and lateral variability was not measured. In contrast, model output can be produced on an arbitrarily small time interval and, despite limited spatial resolution, contains thousands of spatial points due to the inclusion of lateral variability. Although model values are not all statistically independent, the number of degrees of freedom in the model output is much larger than that available in the observational data. In hopes of obtaining reliable statistics, we bin the observational data into intervals of 1 h and 6-m depth, giving approximately 40 measurements per bin. The model data are then binned in the same fashion. Once the statistics have been computed, we employ the Kolmogorov–Smirnov test to determine whether the data are sufficient to distinguish differences between the modeled and observed distributions. We then compare several measures of the central tendency and the spread. Because dissipation rates tend to be distributed lognormally, we employ the common logarithm as the working variable for the statistical analyses. We performed these analyses over two 1-h intervals and one 5-h interval (Figs. 10 ⬤, 11 ⬤, and 12 ⬤), which are representative of the newly developed nocturnal mixed layer. We then examined a 1-h interval following sunrise, in order to quantify the model's reproduction of turbulence decay in the ML (Fig. 13 ⬤). As noted above, dissipation rates observed near the MLB are strongly influenced by heaving motions due to internal waves, a process which the model cannot reproduce. We adjust for this by scaling the depths of measurements by the ratio of measured-to-modeled mixed layer depth. As a result, comparisons are made between water masses that have depths, expressed as a fraction of the mixed layer depth, which are the same.

Despite the generally good qualitative agreement discussed above, quantitative differences are evident in the statistical properties of 6-m samples taken during hours 8 and 13 (Figs. 10 ⊙⚊ and 11 ⊙⚊). The Kolmogorov–Smirnov test indicates that these differences are, for the most part, statistically significant at the 90% confidence level (i.e., the odds that this degree of discrepancy would arise by chance if the underlying distributions were the same are less than 10%). The width of the ε distribution, as measured by the intermittency factor σ_ε, is reproduced very well at most depths. An exception to this occurs near the MLB, where increased σ_ε in the observational results may be a residual effect of vertical motions due to internal waves. The central tendency of ε is not reproduced as well. Three measures of the central tendency, the arithmetic mean, the geometric mean, and the median, all indicate the same conclusion. In the ML, correspondence is generally very good. Below the MLB, measured values exceed modeled values dramatically, that is the decrease in dissipation rates below mixed layer base is significantly larger in the model than in the measurements. We note that the discrepancy is larger during hour 14 than during hour 8, suggesting that it is not an artifact of the finite spinup time for model turbulence. In fact, inspection of Fig. 9a ⊙⚊ reveals that this difference between hours 8 and 14 is due to a temporary increase in turbulence near the ML base, possibly a quasi-random event that the model failed to reproduce.

Statistical comparison of modeled and measured χ tell a similar story (Figs. 10b ⊙⚊ and 11b ⊙⚊). The model reproduces the observed spread of χ quite well. Anomalously large measured intermittency factors near the MLB are due to a few very small measured values. Both observations and model indicate that the intermittency factor for χ tends to exceed that for ε, typically by 20%–30%. In the ML, agreement between central tendencies is relatively good. Below the MLB, measured χ exceeds modeled χ during hour 14, but the discrepancy is in the opposite sense during hour 8.

We now examine the time interval extending from hour 9 to 14 (Fig. 12 ⊙⚊). Averaging over this longer interval eliminates the hour-to-hour variations that appeared in the analyses described above and gives a general view of the relationship between measured and modeled dissipation rates in the nocturnal boundary layer. Some of the evident discrepancies may be due to our imperfect attempts to correct for internal wave effects by scaling depths according to the depth of the ML. For example, changes in turbulence characteristics associated with the MLB appear to occur at a slightly shallower depth (with respect to the MLB) in the model than in the observations. This could be an artifact of our arbitrary definition of the ML depth. The vertical structure of χ below the ML base may also be strongly influenced by large-scale internal wave effects that we do not expect the model to reproduce, as noted above in the discussion of Fig. 9 ⊙⚊. Over this 5-h period, the modeled intermittency factors for both ε and χ agree remarkably well with measurements. The main exception to this occurs in the thermocline, where the model fails to reproduce observed variability in χ (cf. Fig. 9b ⊙⚊). Discrepancies in ε also appear to be robust; the model produces less kinetic energy dissipation than is observed in the thermocline. Note that observational estimates of ε and χ in stratified regions may be too large by a factor of 2 because of anisotropy (Itswiere et al. 1993). Later in this paper, we will assume that the measurements are, in fact, accurate and will argue that the deficiency is due to failure to resolve 1) small-scale Kelvin–Helmholtz (K–H) wave events, and 2) enhanced shear due to large-scale waves. Within the ML, the comparison between central tendencies is relatively close, although observed dissipation rates increase somewhat more rapidly toward the surface than do modeled values. This could be a result of our neglect of surface wave breaking (section 3c).

Following sunrise, ML turbulence is often observed to decay significantly (SMH1). By hour 22 (Fig. 13 ⊙⚊), both ε and χ had decayed in the ML interior by nearly an order of magnitude from the nocturnal values shown in Fig. 12 ⊙⚊. In this case, turbulence decay is clearly magnified by the influence of rain (cf. Smyth et al. 1997). The model reproduces this decay quite well. Below the MLB, however, discrepancies between modeled and measured dissipation rates are even larger during hour 22 than during previous intervals.

The good agreement between model and observations of ε and χ in the ML may be partly a result of our choice of a case with a relatively deep mixed layer and steady surface wind forcing. An extensive comparison of dissipation rates between two observational datasets was made in a similar fashion from data taken 1–11 km apart in the central equatorial Pacific at depths between 15 and 200 m (Moum et al. 1995). Although 3.5-day averages agreed and trends were similar, individual 1-h, 5-m vertical averages differed by up to three orders of magnitude and daily averages by an order of magnitude at some depths. Those results suggest the presence of significant variability in ε on timescales of a few hours and spatial scales of a few kilometers, too large to be captured in the LES model. On this basis, one might expect to see larger differences between observed and modeled ε than we find here. The difference between the current model validation study and the ship intercomparison may be due to both the relatively shallow mixed layer (usually <50 m) and more variable surface wind forcing during the ship study.

5. Resolution of turbulent length scales

Much of the accuracy of LES is dependent on the ability of the model to simulate a significant portion of the turbulent inertial subrange, or the range of length scales where turbulent motions are not directly affected by stratification and shear. With increasing stratification, the scale of energy-containing eddies decreases until the representation of these eddies by LES becomes inaccurate. We believe that this reduction in the characteristic turbulent length scale causes the model to predict ε

and χ incorrectly below the MLB.

Simulated turbulent length scales can be diagnosed by comparing the spectral characteristics of the resolved turbulent motions with theoretical spectra for inertially driven turbulence (Fig. 14 ⊙). Transverse spectra of the horizontal and vertical velocity components, Φ_u, Φ_v, and Φ_w, were obtained by first computing the one-dimensional Fourier transform of each component in the meridional (for u and w) or zonal (for v) direction and then averaging each resulting power spectrum over the remaining horizontal coordinate. By comparing the model-generated spectra with the theoretical Kolmogorov spectrum for isotropic inertially driven turbulence (Schmidt and Schumann 1989), we can determine whether the resolved eddy field is governed by isotropic, inertially driven turbulence, or by stratification and shear stress.

Near the surface, the simulated spectra show the effects of the Langmuir circulations: the vertical velocity has a peak spectral energy at 10–20-m wavelengths that is about a factor of 2 larger than the theoretical spectral energy. At depth 20 and 40 m, the model is clearly resolving a portion of the inertial subrange, as shown by the good correspondence between the simulated spectral curves and the Kolmogorov spectra for all components of velocity. At both depths, the turbulence is nearly isotropic, and the modeled and theoretical amplitudes agree. This is not true at 65 m, where the spectra show considerable variability among the three velocity components. The most energetic spectra at this depth are produced by the horizontal velocity components, suggesting that stratification has produced circulations that are primarily in the horizontal plane. Two features are apparent at 65 m. First, the vertical velocity spectrum falls short of predicted levels, and second, the slopes of the horizontal velocity spectra significantly depart from those predicted for an inertial subrange of turbulence. These features are typical of buoyancy-affected turbulence spectra (e.g., Gargett et al. 1984).

Anisotropy of the simulated turbulence near the surface and at the MLB brings into question the validity of the Métais and Lesieur parameterization, which, like most subgrid-scale models, is designed to simulate the effects of subgrid-scale turbulence only when the resolved flow is isotropic. One of the goals of our research was to determine how critical isotropy is in modeling turbulence with LES. At depth 20 and 40 m, the model clearly simulates an isotropic field of turbulence. This is not true near the upper and lower boundaries of the ML, where anisotropic circulations are caused by boundary proximity and stable stratification, respectively. The anisotropy of these circulations may explain the poor comparison between the modeled and observed dissipation rates. However, this does not prove that the resolved flow properties are incorrect at these depths. In fact, analysis of the heat and salt fluxes in section 6 (below) shows that resolved anisotropic circulations at the MLB produce eddy fluxes consistent with the observations.

The validity of LES for a given flow regime can also be determined using a variety of diagnostic estimates of the energy-containing scales of the turbulence (e.g., Moum 1996a). Two length scales that are easily calculated from the simulation are the Ozmidov scale, defined as

$$L_o = \left(\frac{\varepsilon}{N^3} \right)^{1/2} \qquad (9)$$

and the buoyancy length scale

$$L_b = \frac{w}{N}, \qquad (10)$$

where N is calculated using reordered density to prevent unstable vertical gradients. Both L_o and L_b estimate the maximum size eddies can attain before being attenuated by stratification. In the simulation, averaged values of L_o and L_b have similar profiles, with large values in the almost neutrally stratified mixed layer and a rapid decrease in the upper thermocline (Fig. 15 ⊙). In the mixed layer, L_o and L_b are not a particularly useful measure of turbulent scales because the length scale is set by the mixed layer depth rather than by the stratification. Here L_o and L_b are most representative for turbulence scaling in the upper thermocline where length scales are limited by stratification. Because the methods used to estimate ε from the model output require the existence of a well-resolved inertial subrange, reliable estimates of ε cannot be made where L_o and L_b diminish to the order of the subgrid scale (Fig. 15 ⊙). Note that L_o and L_b both drop below the resolution limit near 65-m depth, which is approximately the depth where good agreement between modeled and measured dissipation rates found in the ML gives way to the poor agreement that is characteristic of the thermocline (cf. section 5). This provides a reasonable explanation for lower model estimates of dissipation rates that are observed in the thermocline region.

A more direct estimate of the dominant eddy size is provided by the Thorpe displacement, which is obtained by reordering a density profile to produce a statically stable configuration (Thorpe 1977). A more rigorous approach, in which the entire three-dimensional density field is reordered, has been described by Winters et al. (1995). Here, we retain the older method in

order to facilitate comparison with field observations. Measured and modeled Thorpe displacements agree very well (Fig. 16 ⊙) and reveal that turbulence in this nocturnal mixed layer is often dominated by eddies large enough to span the entire layer. Like L_o and L_b, the Thorpe displacement decreases to unresolvable size below the mixed layer.

Small values for L_o and L_b do not necessarily affect the horizontal velocity variations shown in Fig. 14 ⊙ at 65-m depth. A number of processes can produce velocity perturbations at the MLB and in the upper pycnocline. The largest horizontal-scale signals can be attributed to mixed layer eddies impinging on the top of the pycnocline, for example, the downward motion at zonal distance of ~ 25 m and meridional distance of ~ 100 m at 20-m depth in Fig. 5 ⊙. These eddies produce an obstacle effect that can lead to smaller-scale internal waves downstream from the disturbance. Downward velocities also cause vertical convergence of horizontal momentum, creating regions of stronger shear at the MLB, which can generate enhanced turbulence through shear production or K-H instability. These effects are demonstrated in the zonal cross section shown in Fig. 17 ⊙. Between the zonal coordinates of 280 and 320 m, downward motion from the mixed layer turbulent eddies produces a region of enhanced vertical current shear centered at ~ 65 m depth. Increased shear at the MLB leads to a reduction in Ri causing small-scale (~ 40 m) waves to amplify via K–H instability. These waves intensify over limited regions, generating increased turbulence at scales nearing the model resolution (i.e., ~ 5 m). Disturbances created by these waves are on occasion able to fully overturn as shown, for example, by the cusp in T at zonal distance of 20 m. Their energy is removed directly by the subgrid-scale parameterization, as indicated by the increased ε in this region.

6. Heat and salinity flux at the mixed layer base

A crucial application of ocean turbulence models is the estimation of vertical property fluxes due to turbulent mixing. Understanding these fluxes is essential in the design of large-scale models, and direct measurement is very difficult. Our goal in this section is to compare fluxes of heat and salinity from the LES model with those estimated from measurements. This comparison is complicated by several factors: First, standard methods for estimating scalar fluxes from microstructure data are only valid in regimes of stable stratification (e.g., SHM2). Also, as we have seen in the previous section, the LES model does not produce accurate turbulence levels in stably stratified flow because of decreased characteristic turbulent length scales. However, the most important fluxes are those that occur in the entrainment zone at the MLB (SHM2). This is a region of moderately stable stratification, where both the observational estimates and the model values of the scalar fluxes may be estimated with reasonable confidence. A third complication stems from the fact that the modeled fluxes, $\overline{w'T'}$ and $\overline{w'S'}$, contain both reversible and irreversible components, whereas the dissipation method used in inferring fluxes from microstructure data estimates the irreversible part only. Accordingly, we compare averages taken over several hours so that the reversible parts of $\overline{w'T'}$ and $\overline{w'S'}$ are effectively filtered out.

Modeled turbulent heat and salinity fluxes at the MLB are presented in Fig. 18 ⊙, along with estimates of the observed fluxes calculated in SHM2. Comparison of the model-resolved fluxes with the observations is remarkably good, considering the uncertainties present in both estimates. Average modeled heat and salinity fluxes were −22.0 W m^{-2} and 2.8 × 10^{-6} psu m s^{-1}, respectively, in comparison with the observed fluxes of −28.3 W m^{-2} and 3.7 × 10^{-6} psu m s^{-1}. Individual hourly estimates do not compare as well as do the 24-h averages. The root-mean-squared (rms) discrepancies between hourly averaged modeled and measured fluxes were 15.4 W m^{-2} for heat and 2.2 × 10^{-6} psu m s^{-1} for salt. For comparison, the uncertainty in observational heat flux estimates, averaged over the entire 3-week cruise, is 10 W m^{-2} (SHM2).

The main discrepancies between the measured and modeled heat fluxes seem to be 1) a long period internal wave effect, as shown by the rise and fall of the observed MLB and heat flux between hours 8 and 15 and 2) a systematic decrease in modeled fluxes after hour 16. It is clear that the relatively small fluxes produced by the model after hour 16 are due to model drift. Turbulence near the MLB is mostly driven by shear, and the turbulence acts to reduce that shear. Profiles of shear presented earlier (Fig. 4 ⊙) demonstrate this effect in the model. The shear and the resulting turbulence decay in time unless some mechanism is present to maintain the shear. In the ocean, a large-scale internal wave that was generated as part of the ocean's response to the westerly wind burst (SHM1) acted to reinforce the shear at the MLB during the latter part of the simulation and thus to maintain the heat flux. That mechanism was not present in the model, and model turbulence near the MLB decayed in the final few hours of the simulation as a result.

If one ignores the time period in which obvious model drift occurred, and considers only the heat and salt fluxes in the period from before hour 16, agreement between model and measurement is significantly improved. Model heat and salt fluxes, averaged between hours 0 and 16, were −21.6 W m^{-2} and 2.8 × 10^{-6} psu m s^{-1}, whereas the corresponding measured fluxes were −23.0 W m^{-2} and 3.1 × 10^{-6} psu m s^{-1}. The rms discrepancies in hourly averaged heat and salt fluxes over this period were 12.5 W m^{-2} and 2.0 × 10^{-6} psu m s^{-1}, respectively. This is an encouraging result given the rather poor comparison between measured and modeled χ in the same region of the flow noted in section 6.

How can the model provide accurate fluxes at the MLB despite its inability to develop realistic small-scale turbulence? Fluxes tend to be driven by the most energetic eddies. For the present case, horizontal cospectra (not shown) have

confirmed that fluxes are driven almost entirely by eddies in the range 30–100 m. Motions on this scale are accurately resolved in our model.

7. Summary and discussion

The response of the ocean surface boundary layer to the WWB observed during COARE was simulated using a three-dimensional ocean LES model. The model results suggest that upper-ocean mixing during a WWB is driven by three main processes, Langmuir circulations, convective instability, and shear instability (although we did not address the effects of surface wave breaking). Each of these processes acts in different parts of the water column and on different spatial scales. For example, surface wave–current interaction produces small-scale turbulent eddies restricted to the upper 10–15 m. Convective instability and shear production act on both the mixed layer depth scale and on a smaller scale associated with K–H waves near the mixed layer base. These three processes can be connected to produce a conceptual model relating the simulated turbulence to measurements of the TKE dissipation rate. Within 10 m of the surface, Langmuir circulations dominate the simulated surface turbulence field and lead to a maximum in the turbulence dissipation rate. In reality, this turbulence is probably enhanced by wave breaking, which is not present in our model. The mixed layer below the surface wave zone exhibits lower dissipation rates and is dominated by mixed layer scale eddies that are generated by both surface buoyancy and wind forcing. Near the bottom of the mixed layer, interaction of mixed layer eddies with the upper-pycnocline shear zone and K–H waves create a second region of high turbulence that is connected with both increased surface momentum forcing and large-scale current disturbances created by the WWB events (SHM1). Kelvin–Helmholtz waves at the MLB are typically limited to a few meters in vertical extent. Close examination of breaking wave events near the mixed layer base suggests that mixed layer entrainment was dominated by K–H wave instability, in contrast with previous modeling studies of low-shear mixed layers showing entrainment by turbulent plumes eroding the upper pycnocline (Skyllingstad and Denbo 1995).

Overall, the model did a good job at simulating the observed features of the mixed layer as shown by comparisons of ε and χ but was unable to accurately predict dissipation rates below the MLB. The model was consistent in showing strong turbulence in the mixed layer at nearly the same time periods as the observations and with similar vertical structure. Initially, the model produced a shallow mixed layer characteristic of a balance between stratification due to surface heating and wind-forced turbulent mixing. With the onset of nighttime cooling, the mixed layer deepened rapidly until it reached an equilibrium near hour 10. Comparison between the model and observations shows good agreement in the mixed layer during this time period, but with lower simulated TKE dissipation rates in the thermocline.

A summary of the model verification is presented in Fig. 19 as a schematic overlaid on a time–depth section of the Ozmidov length scale, taken from the observed fields. Here, we imagine the depth–time range of the simulation as divided into five regions (all boundaries between regions are approximate).

1. In the upper 10 m, comparison is impossible because the observational data is contaminated by ship wake.

2. In the early stages of the simulation, turbulence levels were unrealistically low because of the time required for turbulence to spin up. This time is shortest near the surface because of strong wind forcing.

3. Below the ML, turbulence length scales contract to unresolvable size due to stable stratification. This is indicated by Ozmidov scales smaller than $2\Delta z$.

4. In the later stages of the simulation, the modeled mean profiles drifted away from observed forms due to the absence in the model of large-scale forcing effects that act to sustain the shear near the MLB.

5. In the remaining time–depth region, labeled "optimal comparison," both model and measurements are considered valid.

Comparison of the intermittency factors for ε and χ was almost uniformly good. Within the nocturnal ML (region 5), the means agreed quite well, although the slight tendency for measured dissipation rates to increase more rapidly toward the surface than did their modeled counterparts may be an artifact of the neglect of surface wave breaking in the model or underestimation of the surface wave height in the Stokes drift parameterization. In region 3 (below the MLB), modeled ε was unrealistically low, presumably due to the model's inability to resolve small-scale overturns. Although the MLB lies at the edge of this region, turbulent fluxes of heat and salt at that depth compare remarkably well with observational estimates. These fluxes are driven mainly by motions on scales comparable to L_o (in contrast with the dissipation rates, which operate at smaller scales) and are therefore less sensitive to resolution than are the dissipation rates. In region 4, shear-generated turbulence in the model decayed, whereas observed turbulence was sustained by large-scale forcing effects. Comparisons with data above 10 m (region 1) are impossible because measurements are contaminated by ship wake. In Fig. 14, we see evidence that resolution is inadequate in that region: the spectra at 5 m reveal anisotropy at the smallest resolved scales.

Our efforts to simulate mixing in the oceanic boundary layer in accord with microstructure observations have thus proved successful except for three problems:model drift, absence of surface wave-breaking effects, and underresolution in stably stratified regions. The model drift problem should be straightforward to solve by representing large-scale effects using forcing terms that affect only the mean flow, while still leaving turbulence generation up to the model. For example, this would allow us to maintain the mean shear near the MLB against the effects of mixing, as appears to happen in the observations. Parameterization of wave breaking is an important topic for future research. The problem of decreased length scales in stratified flow is a difficult one, and one with which atmospheric LES researchers have struggled for some time (e.g., Mason 1994). Direct numerical simulations of small-scale turbulence in stratified flow may provide guidance in this area.

Results from LES experiments provide useful information for building improved mixed layer parameterizations. For example, in designing the K-profile model, Large et al. (1994) employed results from a boundary layer LES to generate profiles of eddy viscosity for convective mixing. This approach could be used to extend the Large et al. model to more general ocean mixed layer situations, such as cases with significant surface wave effects (Langmuir circulations) or shear at the MLB. Results from the TKE budget analysis could be used to improve higher-order closure methods, such as the Mellor and Yamada 2.5 model or the more recent parameterization of Kantha and Clayson (1994).

Despite its limitations, we have seen evidence that LES can provide useful information about the ocean boundary layer. Besides illuminating the physics of turbulence in the ML, the model shows significant skill at predicting fluxes of heat and salt between the ML and the thermocline. Knowledge of these fluxes is essential in the design of large-scale ocean and climate models. With appropriate corrections for model drift, LES may ultimately provide a way to estimate these fluxes from large-scale observational data.

REFERENCES

Anis, A., and J. N. Moum, 1995: Surface wave-turbulence interactions: Scaling $\mathcal{E}(z)$ near the surface of the ocean. *J. Phys. Oceanogr.,* **25,** 2025–2045.. Find this article online

Clark, T. L., 1977: A small-scale dynamic model using a terrain-following coordinate transformation. *J. Comput. Phys.,* **24,** 186–215..

Coleman, G. N., J. H. Ferziger, and P. R. Spalart, 1994: A numerical study of the convective boundary layer. *Bound.-Layer Meteor.,* **70,** 247–272..

Collela, P., 1990: Multidimensional upwind methods for hyperbolic conservation laws. *J. Comput. Phys.,* **87,** 171–200..

Craig, P. D., and M. L. Banner, 1994: Modeling wave-enhanced turbulence in the ocean surface layer. *J. Phys. Oceanogr.,* **24,** 2546–2559.. Find this article online

Craik, A. D. D., and S. Leibovich, 1976: A rational model for Langmuir circulations. *J. Fluid Mech.* **73,** 401–426..

Deardorff, J. W., 1980: Stratocumulus-capped mixed layers derived from a three-dimensional model. *Bound.-Layer Meteor.,* **18,** 495–527..

— , and G. E. Willis, 1985: Further results from a laboratory model of the convective planetary boundary layer. *Bound.-Layer Meteor.,* **32,** 205–236..

Denbo, D. W., and E. D. Skyllingstad, 1996: An ocean large-eddy simulation model with application to deep convection in the Greenland Sea. *J. Geophys. Res.,* **101,** 1095–1110..

Durran, D. R., 1991: The third-order Adams–Bashforth method: An attractive alternative to leapfrog time differencing. *Mon. Wea. Rev.,* **119,** 702–720.. Find this article online

Gargett, A. E., T. R. Osborn, and P. W. Nasmyth, 1984: Local isotropy and the decay of turbulence in a stratified turbulence. *J. Fluid Mech.,* **144,** 231–280..

Garwood, R. W., 1977: An ocean mixed layer model capable of simulating cyclic states. *J. Phys. Oceanogr., 7,* 455–468.. Find this article online

Itswiere, E. C., J. R. Koseff, D. A. Briggs, and J. H. Ferziger, 1993:Turbulence in stratified shear flows: Implications for interpreting shear-induced mixing in the ocean. *J. Phys. Oceanogr., 23,* 1508–1522.. Find this article online

Kaimal, J. C., J. C. Wyngaard, D. A. Haugen, O. R. Coté, Y. Izumi, S. J. Caughey, and C. J. Readings, 1976: Turbulence structure in the convective boundary layer. *J. Atmos. Sci., 33,* 2152–2169.. Find this article online

Kantha, L. H., and C. A. Clayson, 1994: An improved mixed layer model for geophysical applications. *J. Geophys. Res., 99,* 25 235–25 266..

Kraus, E. B., and J. S. Turner, 1967: A one-dimensional model of the seasonal thermocline, II, The general theory and its consequences. *Tellus, 19,* 98–105..

Large, W. G., J. C. McWilliams, and S. C. Doney, 1994: Oceanic vertical mixing: A review and a model with a nonlocal boundary layer parameterization. *Rev. Geophys., 32,* 363–403..

Lenschow, D. H., J. C. Wyngaard, and W. T. Pennell, 1980: Mean-field and second-moment budgets in a baroclinic, convective boundary layer. *J. Atmos. Sci., 37,* 1313–1326.. Find this article online

Leveque, R., 1996: High-resolution conservative algorithms for advection in incompressible flow. *SIAM J. Numer. Anal., 33,* 627–665..

Li, M., and C. Garrett, 1993: Cell merging and the jet/downwelling ratio in Langmuir circulation. *J. Mar. Res., 51,* 737–769..

Mason, P. J., 1994: Large-eddy simulation: A critical review of the technique. *Quart. J. Roy. Meteor. Soc., 120,* 1–26..

McWilliams, J. C., P. P. Sullivan, and C.-H. Moeng, 1997: Langmuir turbulence in the ocean. *J. Fluid Mech., 334,* 1–30..

Mellor, G. L., and T. Yamada, 1982: Development of a turbulence closure for geophysical fluid problems. *Rev. Geophys., 20,* 851–875..

Métais, O., and M. Lesieur, 1992. Spectral large-eddy simulations of isotropic and stably stratified turbulence. *J. Fluid Mech., 239,* 157–194..

Moeng, C.-H., and P. P. Sullivan, 1994: A comparison of shear and buoyancy driven planetary boundary flows. *J. Atmos. Sci., 51,* 999–1022.. Find this article online

Moum, J. N., 1996a: Energy-containing scales of turbulence in the ocean thermocline. *J. Geophys. Res., 101,* 14 095–14 109..

—— ,1996b: Efficiency of mixing in the main thermocline, *J. Geophys. Res., 101,* 12 057–12 069..

—— ,M. C. Gregg, R. C. Lien, and M. E. Carr, 1995: Comparison of turbulence kinetic energy dissipation rates from two ocean microstructure profilers. *J. Atmos. Oceanic Technol., 12,* 346–366..

Price, J. F., R. A. Weller, and R. Pinkel, 1986: Diurnal cycling: Observations and models of the upper ocean response to diurnal heating, cooling, and wind mixing. *J. Geophys. Res., 91,* 8411–8427..

Schmidt, H., and U. Schumann, 1989: Coherent structure of the convective boundary layer derived from large-eddy simulations. *J. Fluid Mech., 200,* 511–562..

Shay, T. J., and M. C. Gregg, 1986: Convectively driven turbulent mixing in the upper ocean. *J. Phys. Oceanogr., 16,* 1777–1798.. Find this article online

Siegel, D. A., and A. Domaradzki, 1994: Large-eddy simulation of decaying stably stratified turbulence. *J. Phys. Oceanogr., 24,* 2353–2386.. Find this article online

—— ,J. C. Ohlmann, L. Washburn, R. R. Bidigare, C. T. Nosse, E. Fields, and Y. Zhou, 1995: Solar radiation, phytoplankton pigments and the radiant heating of the equatorial Pacific warm pool. *J. Geophys. Res., 100,* 4885–4891..

Skyllingstad, E. D., and D. W. Denbo, 1995: An ocean large-eddy simulation of Langmuir circulations and convection in the surface mixed layer. *J. Geophys. Res., 100,* 8501–8522..

—— ,T. Paluszkiewicz, D. W. Denbo, and W. D. Smyth, 1996: Nonlinear vertical mixing processes in the ocean: modeling and parameterization. *Physica D, 98,* 574–593..

Smyth, W. D., D. Hebert, and J. N. Mourn, 1996a: Local ocean response to a multiphase westerly windburst. Part 1: The dynamic

response. *J. Geophys. Res.,* **101,** 22 495–22 512..

— ,— ,and — ,1996b: Local ocean response to a multiphase westerly windburst. Part 2: Thermal and freshwater responses. *J. Geophys. Res.,* **101,** 22 513–22 533..

— ,P. O. Zavialov, and J. N. Moum, 1997: Decay of turbulence in the upper ocean following sudden isolation from surface forcing. *J. Phys. Oceanogr.,* **27,** 810–822.. Find this article online

Terray, E. A., M. A. Donelan, Y. C. Agrawal, W. M. Drennan, K. K. Kahma, A. J. Williams III, P. A. Hwang, and S. A. Kitaigorodskii, 1996: Estimates of kinetic energy dissipation under breaking waves. *J. Phys. Oceanogr.,* **26,** 792–807.. Find this article online

Thorpe, S. A., 1977: Turbulence and mixing in a Scottish loch. *Philos. Trans. Roy. Soc. London Ser. A,* **286,** 125–181..

UNESCO (United Nations Educational, Scientific, and Cultural Organization), 1981: Tenth Report on the Joint Panel of Oceanographic Tables and Standards (1981). UNESCO Tech. Papers in Mar. Sci., No. 30..

Wang, D., W. G. Large, and J. C. McWilliams, 1996: Large-eddy simulation of the equatorial ocean boundary layer: Diurnal cycling, eddy viscosity, and horizontal rotation. *J. Geophys. Res.,* **101,** 3649–3662..

— ,J. C. McWilliams, and W. G. Large, 1998: Large eddy simulation of the diurnal cycle of deep equatorial turbulence. *J. Phys. Oceanogr.,* **28,** 129–148.. Find this article online

Wijesekera, H. W., and M. C. Gregg, 1996: Surface layer response to weak winds, westerly bursts, and rain squalls in the western Pacific warm pool. *J. Geophys. Res.,* **101,** 977–997..

Winters, K. B., P. N. Lombard, J. J. Riley, and E. A. D'Asaro, 1995:Available potential energy and mixing in density-stratified fluids. *J. Fluid Mech.,* **289,** 115–128..

Wyngaard, J. C., and L. J. Peltier, 1996: Experimental micrometeorology in an era of turbulence simulation. *Bound.-Layer Meteor.,* **78,** 71–86..

APPENDIX

8. Calculation of Turbulent Dissipation Rates

Neither of the turbulent dissipation rates, ε and χ, are calculated directly by the LES model. Instead, they are inferred, using assumptions that are consistent with those upon which the subgrid-scale model is based. The foremost of these is that the smallest resolved scale lies within an inertial subrange. Each of the dissipation rates can be calculated in one of two ways. The first method follows directly from the structure function SGS model. The second method requires fitting a portion of the modeled spectrum to the theoretical form. In this appendix, we describe and compare these methods. Because they are simpler, we begin with the methods available for the calculation of χ.

In homogeneous, isotropic turbulence, the structure function for the temperature may be expressed as

$$F_T(\mathbf{r}) = \overline{[T(\mathbf{x} + \mathbf{r}) - T(\mathbf{x})]^2}$$

$$= 4 \int_0^\infty E_T(k)\left(1 - \frac{\sin kr}{kr}\right) dk \qquad \text{(A1)}$$

in which the overbar denotes a spatial average, $E_T(k)$ is the temperature variance spectrum, k is the radial wavenumber, and $r = |\mathbf{r}|$.

In the equilibrium range, the spectrum is given by

$$E_T(k) = \beta \frac{\chi}{2} \varepsilon^{-1/3} k^{-5/3}. \qquad \text{(A2)}$$

The constant β is given the value 0.8. Substituting (A2) into (A1) and integrating, we obtain

$$F_T(\mathbf{r}) = 2.41\beta\chi(r^2/\varepsilon)^{1/3}.$$

We now substitute $r = \Delta = (\Delta x \Delta y \Delta z)^{1/3}$ and solve for χ,

$$\chi = \frac{1}{2.41\beta}F_T(\Delta)\left(\frac{\varepsilon}{\Delta^2}\right)^{1/3}. \tag{A3}$$

Finally, we must account for the fact that $\overline{F}_T$, our estimate of the temperature structure function, is based on resolved temperature fluctuations only. In effect, the integral in (A1) extends not to $k = \infty$, but only to $k = \pi/\Delta$. The required correction has been derived by Métais and Lesieur (1992):

$$F_T(\Delta) = 2.53\overline{F}_T(\Delta). \tag{A4}$$

The formula for χ_{sf}, the estimate of χ based on the structure function, is now obtained by substituting (A4) into (A3):

$$\chi_{sf} = \frac{1.05}{\beta}\overline{F}_T(\Delta)\left(\frac{\varepsilon}{\Delta^2}\right)^{1/3}. \tag{A5}$$

The second estimate of χ is obtained by assuming that the meridional temperature variance spectrum between wavelengths of 64Δ to 3Δ has the form (A2). We then solve for χ at each wavenumber

$$\chi_{sp} = \frac{2\varepsilon_{sf}^{1/3}}{\beta}k^{5/3}E_T(k) \tag{A6}$$

and average the results over the wavenumbers $2\pi/64\Delta$–$2\pi/3\Delta$. The TKE dissipation rate ε_{sf} is defined below.

We turn now to the analogous methods for estimating ε. The estimate based on the velocity structure function is derived in a manner similar to the derivation of χ_{sf} given above. Details may be found in Métais and Lesieur [1992, cf. Eqs. (5.21) and (5.31)]. The result is

$$\varepsilon_{sf} = \frac{0.38}{\Delta}\left(\frac{\overline{F}(\Delta)}{C_k}\right)^{3/2}. \tag{A7}$$

The Kolmogorov constant C_k is given the value 1.4. We fit the transverse velocity variance spectrum to the standard form for the inertial subrange to obtain

$$\varepsilon_{u,w} = \left[\frac{3}{4\alpha_1}k_2^{5/3}\Phi_{u,w}(k_2)\right]^{3/2} \tag{A8}$$

and average over the wavenumber range $2\pi/64\Delta$–$2\pi/3\Delta$ as before. Note that either u or w may be used for the velocity component in (A8). The value of the constant α_1 is given by $(18/55)C_k = 0.46$.

Estimates of ε and χ derived using the above methods are presented in Fig. A1 ⊙ from hour 8. For ε in the upper half of the mixed layer, the two estimation methods yield similar profiles. The exception is the u spectrum method, which underestimates ε because of anisotropic Langmuir circulations. The good agreement between the subgrid scale and the w spectral methods is expected, given that this region of the mixed layer behaves much like a convective boundary layer with the peak energy in the largest turbulent eddies, a situation well suited for the application of LES. In contrast, the bottom half of the mixed layer shows larger differences between the ε estimates, with the higher values produced by the u spectral method. In this part of the mixed layer, K–H instability dominates the mixing process and tends to force small-scale anisotropic disturbances that have a skewed vertical velocity spectrum, causing a reduction in ε when using the w spectral technique. Underestimation of χ by the spectral method in the thermocline is probably due to reduced vertical variability of T variance. In general, these plots indicate that the structure function form for ε and χ, which are used in our validation

comparisons, yield dissipation rate estimates in the ML that are consistent with a resolved inertial subrange of turbulence.

Figures
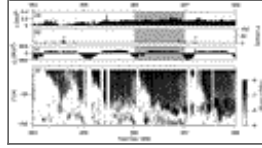
Fig. 1. (a) Surface wind stress, (b) precipitation, (c) net surface heat flux, and (d) turbulent kinetic energy dissipation rate, observed during a 4-day section of the COARE Intensive Observation Period. The shaded time period represents the simulation presented in the text (day 366).
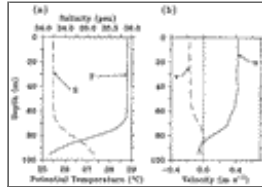
Fig. 2. Data used to define initial and upper boundary conditions. (a) Potential temperature and salinity and (b) zonal and meridional velocity taken from measurements made on 31 December 1992 at 0000 UTC. Profiles are 1-h averages of the observations centered on 0000 UTC.
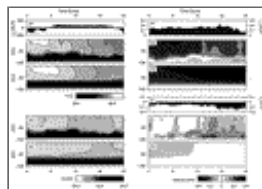
Fig. 3. (a) Time series of observed surface heat fluxes. Time–depth sections of observed (b) and modeled (c) temperature, observed (d) and modeled (e) salinity. Observed zonal surface wind stress (f) and observed (g) and modeled (h) zonal velocity. Observed meridional surface wind stress (i) and observed (j) and modeled (k) meridional velocity. Observations of oceanic variables are binned over 4 m in depth and over 6 min in time. Time averaging is accomplished using a moving triangular window of length 36 min. Model profiles are horizontally averaged every 6 min. Also shown are the mixed layer depths from the model (solid white curve) and measurements (white points).
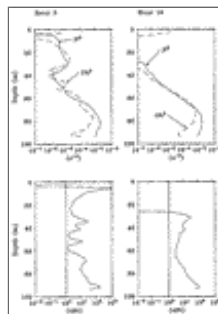
Fig. 4. Squared Brunt–Väisälä frequency, squared shear and Richardson number profiles taken from the simulation at hours 3 and 16. Richardson number of ¼ is indicated by the vertical line.
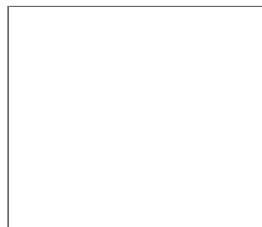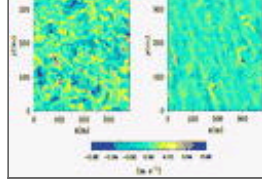
Fig. 5. Horizontal cross sections of the vertical velocity at depths (a) 5, (b) 20, (c) 40, and (d) 65 m taken from the simulation at hour 8. The arrow in (a) is the wind direction.
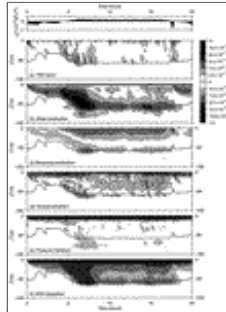
Fig. 6. Time–depth sections of the largest terms in the resolved turbulent kinetic energy budget (6) along with the surface buoyancy flux $J^o{}_b$. Also shown is the mixed layer depth (solid line). All TKE budget terms are in units of W kg^{-1}.
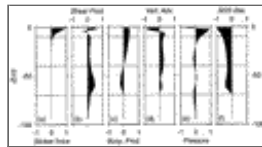
Fig. 7. Time-averaged profiles of the turbulent kinetic energy budget terms corresponding to Fig. 6 for hours 11–20. Also shown is the time-averaged Stokes vortex force term (not shown in Fig. 6). Each quantity is scaled using $\Psi' = \Psi/(a + |\Psi|)$, where Ψ is the TKE budget term and $a = 2 \times 10^{-7}$.
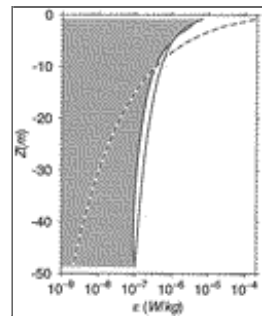
Fig. 8. Dissipation rates at hour 8. Model is shaded, surface layer scaling (8) is solid, and Craig and Banner scaling (7) is dashed.

Fig. 9. Time–depth sections of (a) the TKE dissipation rate $\mathcal{E}$ and (b) the temperature variance dissipation rate χ. In each case, the upper frame shows profiles taken from the model output at a fixed horizontal location, while the lower frame shows individual profiles measured by the microstructure profiler. The base of the mixed layer, defined as the depth where the density first exceeds its surface value by .01 kg m^{-2}, is indicated by white circles for the measurements, and by a white line for the simulation. To aid in visual comparison, the upper limit of the observational data (above which values are contaminated by ship wake) is shown on the model diagrams with a thin horizontal white line at 10-m depth.
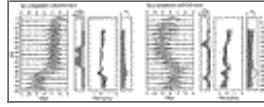
Fig. 10. Statistics of measured and modeled dissipation rates [(a) $\mathcal{E}$, (b) χ] during hour 8. In the leftmost frame, histograms indicate the distribution of modeled dissipation rates over all horizontal locations and 6 m of depth. Points indicate 1-m averages derived from microstructure measurements. The depths at which the points appear have been multiplied by the ratio of modeled to measured ML depth, to correct for vertical advection by unresolved internal wave motions. The second frame shows the result of the Kolmogorov–Smirnov test. When 1-PKS > 0.9, the chances are less than 10% that samples of this size drawn from two identical distributions would differ to the degree observed (i.e., the observed difference in probability distributions is significant at the 90% level). The third frame gives the discrepancy (measured minus modeled) in three measures of the central tendency: the median (shaded curve), the geometric mean (solid curve), and the arithmetic mean (dashed curve). The far right frame shows the intermittency factor (the standard deviation of the logarithm). The filled curve is the model value; the dashed curve represents the measured data.
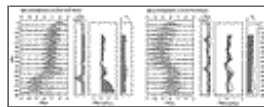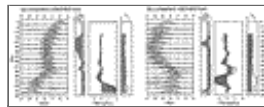
Fig. 11. Same as Fig. 10 but for hour 14.
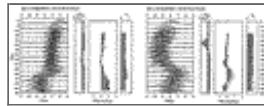
Fig. 12. Same as Fig. 10 but for the 5-h period spanning hours 9–13, inclusive.

Fig. 13. Same as Fig. 10 but for hour 22.
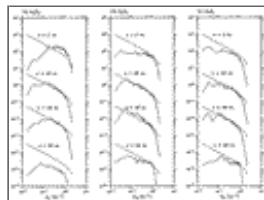
Fig. 14. Horizontal spectra Φ at 5-, 20-, 40-, and 65-m depth for w, u, and υ at hour 8, scaled by the wavenumber k_x and k_y, where $k = 2\pi/\lambda$ with λ being the horizontal wavelength in the x or y direction. Also shown are Kolmogorov spectra (described in the appendix) for isotropic inertially driven turbulence, adjusted for a finite-difference grid at scales less than $4\Delta x$ (see Schmidt and Schumann 1986) using the subgrid-scale model $\mathcal{E}_{sf}$ (defined in the appendix). For consistency, spectra for u and w are taken in the meridional direction and averaged zonally, and the spectrum for υ is taken in the zonal direction and averaged meridionally. Spectra at 40, 20, and 5 m are scaled by factors of 10^2, 10^4, and 10^6, respectively.
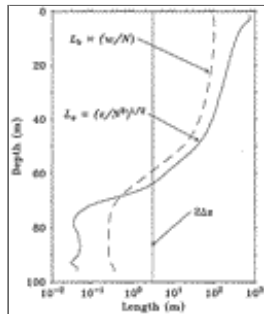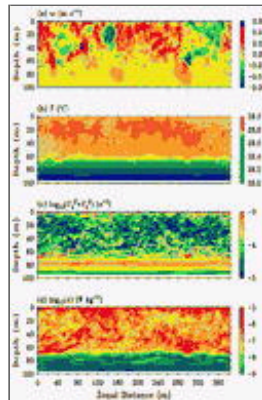
Click on thumbnail for full-sized image.

Fig. 15. Horizontally averaged Ozmidov length scale (L_o) and buoyancy length scale (L_b) taken from the model at hour 8.
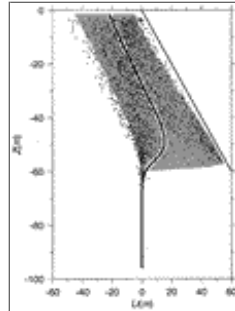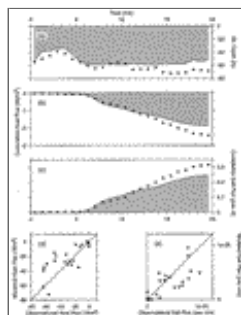

Click on thumbnail for full-sized image.

Fig. 16. Mean (solid curve) and 95% confidence intervals of the Thorpe displacement (LT) taken from the model for hours 8–14 inclusive. Points indicate observed values for the same time period, with depths scaled to remove the effects of unresolved wave motions on the MLB. Also shown is the maximum possible Thorpe scale (thin straight line).
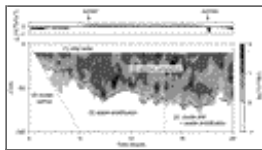

Click on thumbnail for full-sized image.

Fig. 17. Zonal cross section of simulated (a) vertical velocity, (b) temperature, (c) vertical current shear, and (d) TKE dissipation rate taken from meridional distance of 150 m at hour 8.
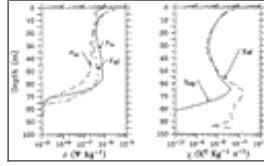

Click on thumbnail for full-sized image.

Fig. 18. Comparison of modeled and observational estimates of heat and salinity fluxes at the mixed layer base. (a) Mixed layer depth, defined as the depth over which density exceeds its surface value by less than .01 kg m^{-3}, (b) cumulative heat flux across the MLB, and (c) cumulative salt flux across the MLB. In (a), (b), and (c), the shaded curve represents the modeled value, whereas asterisks represent observational estimates (from SHM2). All data is binned into 1-h averages. The bottom panels show hourly averaged modeled versus observational flux estimates: (d) heat flux, (e) salt flux.

Click on thumbnail for full-sized image.

Fig. 19. Factors that determine the success of model-measurement comparisons. For reference, the surface buoyancy flux is shown in the upper frame. Shading indicates the (measured) Ozmidov scale, $L_o = (\varepsilon/N^3)^{1/2}$. Black dots indicate the base of the mixed layer.

Click on thumbnail for full-sized image.

Fig. A1. Estimates of the turbulent dissipation rates of kinetic energy and temperature variance, ε and χ, derived by fitting the horizontally averaged spectra of w and u for ε (labeled w and u), and T for χ (labeled **sp**), to a theoretical Kolmogorov spectrum, as described in the text. Also shown are ε and χ estimates made using the Métais and Lesieur subgrid parameterization (labeled **sf**).

Corresponding author address: Dr. Eric D. Skyllingstad, College of Oceanic and Atmospheric Sciences, Oregon State University, 104 Ocean Admin. Bldg., Corvallis, OR 97331.

E-mail: skylling@oce.orst.edu